How do normal faults grow above dykes?

Craig Magee[1]*, Christopher A-L Jackson[2]

[1]Institute of Geophysics and Tectonics, School of Earth Science and Environment, University

of Leeds, Leeds, LS2 9JT, UK

[2]Basins Research Group, Department of Earth Science and Engineering, Imperial College

London, London, SW7 2BP, UK

*corresponding author: c.magee@leeds.ac.uk

Dykes feed volcanic eruptions and drive crustal extension on Earth and other planetary bodies. Yet many dykes do not reach the surface, but induce normal faulting of overlying rock. Whilst such dyke-induced faults provide an accessible surficial record of active and ancient dyking, unlocking these archives is difficult because we do not know how faults grow above or geometrically relate to dykes in 3D. Here we use seismic reflection images to quantify the 3D structure and kinematics of natural dyke-induced normal faults for the first time. We show variations in fault dip and displacement distribution control the surface expression of dyke-induced faults. High-displacement zones occur along fault-strike, suggesting isolated fault segments nucleated between the dyke upper tip and surface during dyke propagation. Periods of dyke stalling and thickening prompted fault segment growth and linkage. Our results demonstrate at-surface measurements of dyke-induced faults cannot be used to estimate dyke parameters without a priori knowledge of fault kinematics. We show reflection seismology is a powerful tool for studying how faults grow above dykes, and anticipate

future seismic-based studies will improve our understanding of dyke emplacement and its translation into surface deformation.

Field observations, geodetic data, and seismicity show dyke intrusion can induce normal faulting of overlying rocks [*Mastin and Pollard*, 1988; *Passarelli et al.*, 2015; *Pollard et al.*, 1983; *Rubin*, 1992; *Rubin and Pollard*, 1988; *Sigmundsson et al.*, 2015; *Wright et al.*, 2012; *Xu et al.*, 2016]. Dyke-induced normal faults, henceforth dyke-induced faults, form conjugate pairs that dip towards underlying dykes and bound dyke-parallel graben (Fig. 1) [*Mastin and Pollard*, 1988; *Pollard et al.*, 1983; *Rubin*, 1992; *Trippanera et al.*, 2015a; *Trippanera et al.*, 2015b]. Faulting occurs because dyke intrusion and dilation perturbs the stress state in the overburden, broadly concentrating tensile stress in two lobes above the dyke tip and two zones at the free surface; this complex stress field locally increases the differential stress (σ_1-σ_3) and promotes shear failure (Fig. 1) [*Koehn et al.*, 2019; *Pollard et al.*, 1983; *Rubin*, 1992; *Rubin and Pollard*, 1988]. Vertical fractures may form near the free surface if the reduced lithostatic load (σ_1) favours tensile failure (e.g., Fig. 1a) [*Al Shehri and Gudmundsson*, 2018; *Trippanera et al.*, 2015a]. Because dyking drives the stress changes governing faulting, dyke emplacement and shape thus control, and are reflected in, the growth and geometry of dyke-induced faults [*Dumont et al.*, 2016; *Dumont et al.*, 2017; *Pallister et al.*, 2010; *Pollard et al.*, 1983; *Rubin and Pollard*, 1988]. For example, extension accommodated by dyke-induced faults is sensitive to dyke width, implying fault heave relates to dyke thickness [*Rubin*, 1992; *Rubin and Pollard*, 1988; *Trippanera et al.*, 2015a]. By inverting dyke-induced fault properties (e.g. heave) we can: (i) track and quantify intruding dykes [*Pallister et al.*, 2010]; (ii) determine how faulting influences dyke ascent and eruption [*Maccaferri et al.*, 2016; *Rivalta et al.*, 2015]; (iii) estimate dyke volumes to infer melt conditions [*Wilson and Head*, 2002]; and (iv) examine how dyking shapes Earth [*Carbotte et al.*, 2006; *Ruch et al.*, 2016;

Wright et al., 2012] and other planetary bodies [*Schultz et al.*, 2004; *Wilson and Head*, 2002]. However, exactly how faults relate to dykes remains unclear because we cannot view natural examples in 3D. We are restricted to investigating surface expressions of natural dyke-induced fault [*Dumont et al.*, 2016; *Rubin and Pollard*, 1988; *Schultz et al.*, 2004; *Trippanera et al.*, 2015b; *Wilson and Head*, 2002], meaning 3D models of dyke-induced fault systems cannot easily be verified [*Hardy*, 2016; *Koehn et al.*, 2019; *Mastin and Pollard*, 1988; *Pollard et al.*, 1983; *Trippanera et al.*, 2015a]. Inverting dyke-induced fault properties to recover dyke emplacement and shape therefore relies on assumptions describing 3D fault-dyke relationships that are difficult to test.

Recognition of dykes and dyke-induced faults in seismic reflection data [*Bosworth et al.*, 2015] means we can now examine their 3D structure. Using seismic data, we identify a swarm of dykes and overlying faults offshore NW Australia, and present the first 3D analysis quantifying relationships between natural dykes and dyke-induced faults. We test suggestions that graben half-width (*HW*) geometrically relates to and can be used to predict dyke depth (*D'*), which typically relies on extrapolating fault dips (α) measured at the free surface to depth (i.e. $D' = HW \tan \alpha$) [*Hjartardóttir et al.*, 2016; *Trippanera et al.*, 2015a; *Wilson and Head*, 2002]. Our data also informs debate surrounding the vertical extent of dyke-induced faults and where they nucleate [*Koehn et al.*, 2019; *Rubin*, 1992; *Trippanera et al.*, 2015a]. For example, it is hypothesised dyke-induced faults nucleate either: (i) as near-surface vertical fractures, which transition into faults as they propagate downwards (Fig. 1a) [*Al Shehri and Gudmundsson*, 2018; *Trippanera et al.*, 2015a; *Trippanera et al.*, 2015b]; (ii) at dyke tips before propagating upwards (Fig. 1b)[*Koehn et al.*, 2019; *Rubin*, 1992; *Xu et al.*, 2016]; (iii) a combination of (i) and (ii), with fault segments growing towards each other and linking (Fig. 1c) [*Rowland et al.*, 2007; *Tentler*, 2005]; (iv) between the dyke tip and surface [*Koehn et al.*, 2019; *Mastin and Pollard*, 1988] (e.g. Figs 1d); or (v) in front of a laterally

4

propagating dyke, eventually being cross-cut by the dyke (Fig. 1e) [*Rowland et al.*, 2007; *Rubin and Pollard*, 1988]. These hypotheses can be used to predict diagnostic fault displacement-depth trends if we consider displacement is greatest where faults nucleate (Fig. 1) [*Magee et al.*, 2019]. This assumption is supported by three-dimensional numerical models, which show areas where tectonic faults are active longest typically accrue most displacement [*Deng et al.*, 2017]. Similarly, physical models have demonstrated that the site of displacement maxima on dyke-induced faults formed at the free surface coincides with where the faults nucleated (e.g. Fig. 1a) [*Trippanera et al.*, 2015a]. Measuring 3D displacement patterns across dyke-induced faults allows us to reconstruct their kinematics, which we can relate to dyke thickness changes and emplacement mechanics.
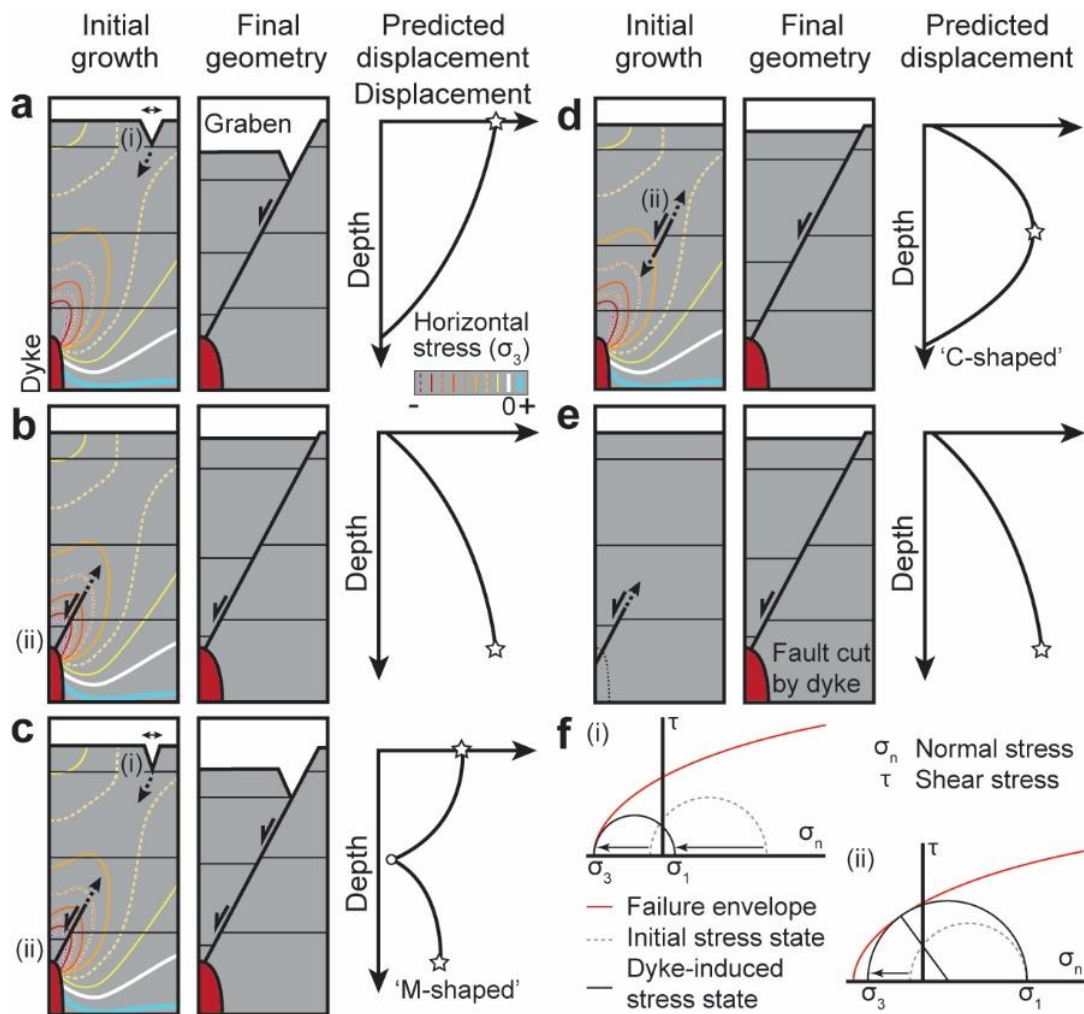
Figure 1: Predicted displacement patterns for different models of dyke-induced faulting.
Hypotheses suggest faults nucleate either: **a,** at the surface [*Al Shehri and Gudmundsson*,
2018; *Trippanera et al.*, 2015a; *Trippanera et al.*, 2015b]; **b,** at the dyke tip [*Koehn et al.*,
2019; *Rubin*, 1992; *Xu et al.*, 2016]; **c,** at the surface and dyke tip [*Rowland et al.*, 2007;
Tentler, 2005]; **d,** between the surface and dyke tip [*Koehn et al.*, 2019; *Mastin and Pollard*,
1988]; or **e,** in front of a laterally propagating dyke [*Rowland et al.*, 2007; *Rubin and Pollard*,
1988]. **f,** Reduction in horizontal stress (σ_3) to negative (tensile) values above intruding dykes
[*Rubin and Pollard*, 1988], which near-surface is coupled with a decrease in lithostatic load
(σ_1), promote failure.

Dykes and dyke-induced faults in seismic reflection data

We map an unrecognised swarm of ~NNE-striking dykes (the Exmouth Dyke Swarm),
emplaced within Triassic clastic rocks of the Mungaroo Formation, using 2D and 3D seismic
data from the Exmouth Plateau (Fig. 2). The nine dykes mapped in the study area manifest as
broadly planar, >9–1.5 km high, up to >80 km long, <300 m wide zones that dim the
brightness (amplitude) of and disrupt otherwise sub-horizontal stratigraphic reflections (Figs
2a, b). We interpret these narrow, low-amplitude zones as dykes, or packages of closely
spaced dykes [*Phillips et al.*, 2018; *Wall et al.*, 2010], because they: (i) occur across multiple
surveys with different processing histories, implying they are not geophysical artefacts (Fig.
2a) [*Phillips et al.*, 2018]; (ii) cross-cut but do not laterally offset channels, indicating they
are not strike-slip faults (e.g. Fig. 2a); and (iii) have a narrow, vertical, low-amplitude seismic
character, which is similar to vertical dykes inferred in other seismic datasets [*Bosworth et
al.*, 2015; *Wall et al.*, 2010].

Above and parallel to the dykes are nine, ~NNE-trending, ~1–2 km wide graben
bound by low-displacement (i.e. <150 m), conjugate normal faults (Fig. 2). There are no

channels offset by the faults that could be used to determine whether there was any component of oblique slip, so we assume displacement was dip-slip. The faults displace a ~1 km thick Triassic-to-Early Cretaceous clastic-dominated sequence, which includes the Near Base Cretaceous unconformity (horizon HK; Fig. 2b) [*Exon et al.*, 1982; *Reeve et al.*, 2016]. Individual faults are continuous or visibly segmented along-strike and dip inwards (at ~45°) to converge at the upper tips of underlying dykes (Figs 2b, c); the faults do not intersect dyke walls [*Rubin and Pollard*, 1988]. We suggest dyking triggered formation of these faults, based on their spatial relationship to inferred dykes and plan-view similarity (i.e. linear, long, and low-displacement) to confirmed dyke-induced faults in Afar[*Dumont et al.*, 2016; *Dumont et al.*, 2017; *Rowland et al.*, 2007], Iceland [*Hjartardóttir et al.*, 2016], and those created in physical and numerical models [*Hardy*, 2016; *Mastin and Pollard*, 1988; *Trippanera et al.*, 2015a]. Displacement of HK at the top of the dyke-induced faults indicates faulting, and thus dyking, occurred during Early Cretaceous rifting and break-up of the NW Australian margin [*Driscoll and Karner*, 1998; *Exon et al.*, 1982; *Reeve et al.*, 2016], coincident with sill emplacement and volcanism[*Symonds et al.*, 1998].

To understand how the observed dyke-induced faults grew above and geometrically relate to dykes, we examine an ~18 km long section of a graben bound by two faults (EF1 and EF2) and underlain by Dyke E (Fig. 2). Subtle but abrupt changes in strike of Dyke E occur along its length, sub-dividing it into sections with trends of 007°, 014°, and 004°; the northernmost dyke section extends for >5 km beyond the seismically resolved portion of the faults (Figs 2, 3a-d). The top of Dyke E, onto which EF1 and EF2 broadly converge, is located at a current depth of ~3.5±0.6 km (Figs 2b, 3b). We cannot resolve whether Dyke E consists of one or multiple, closely space dykes. The width of the low-amplitude zone marking Dyke E, which probably does not correspond to true dyke or cumulative thickness [*Wall et al.*, 2010] but can be considered a proxy for relative thickness trends, gradually

decreases northwards (Fig. 3a, b). In the south of the study area, Dyke E extends below the survey limit, but dyke height appears to decrease northwards of ~8.75 km in a step-wise manner from >5±1.2 km to ~1.7±0.9 km as the depth to the dyke(s) base decreases (Fig. 3b). The apparent northwards decrease in the width and height of the dykes' geophysical expression suggest it may have propagated laterally from south to north.
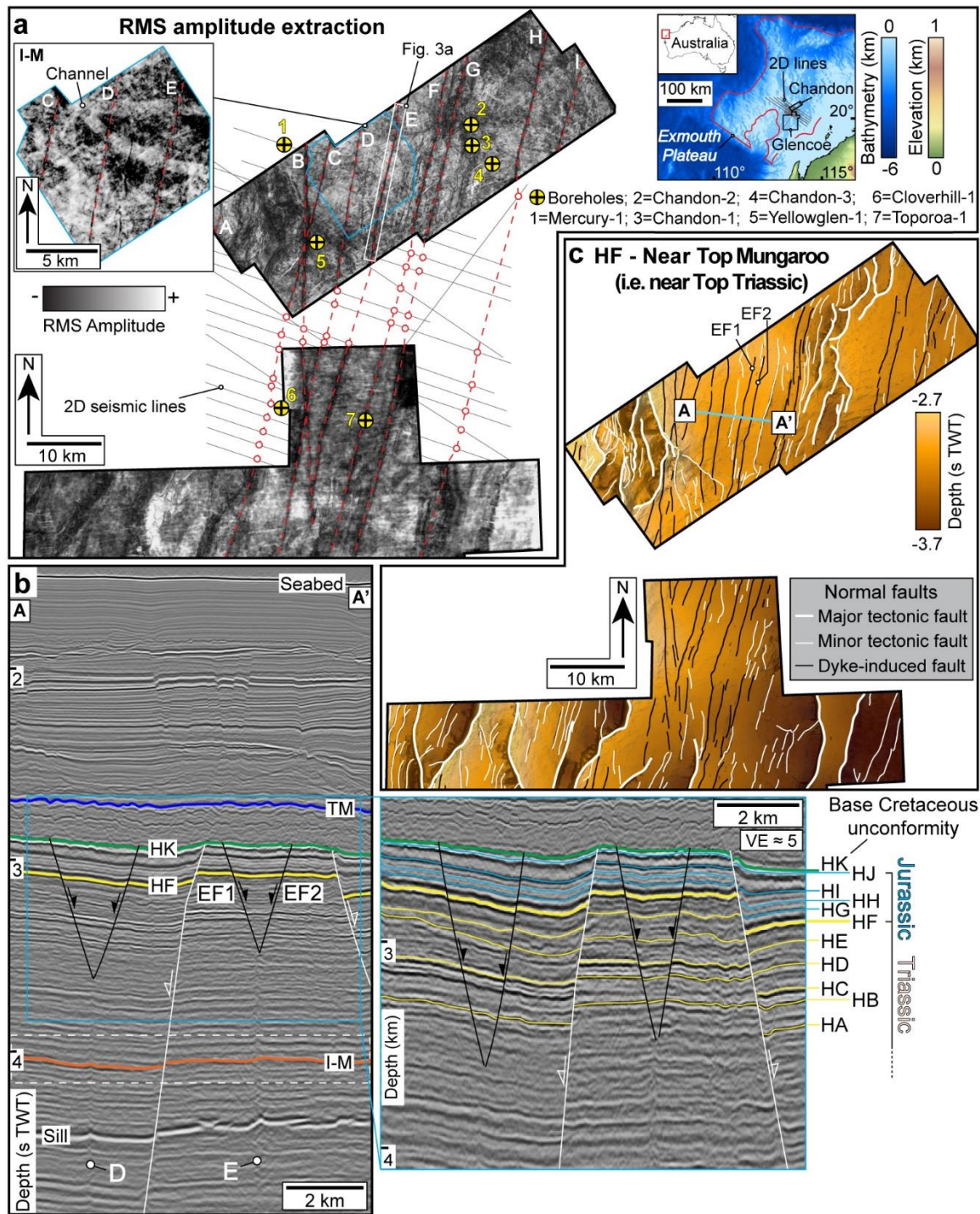
Figure 2: Dykes and dyke-induced faults imaged in seismic reflection data from Exmouth Plateau, offshore NW Australia. See Supplementary Figure 1 for uninterpreted version of this figure and Supplementary Video 1 for a 3D view of the seismic data and interpretations. **a,** Root-mean squared (RMS) amplitude extraction across a ~0.2 km high window (dashed white line in **b,**) at ~4 km depth showing dyke A–I traces. Inset: RMS amplitude map

showing channels along I-M horizon (see **b,**) are not offset by dykes. **b,** Time-migrated (in seconds two-way time (TWT)) and a vertically exaggerated (VE), depth-converted seismic section showing dykes, faults, and key horizons. See **c,** for location. **c,** HF time-structure map highlighting plan-view morphologies of tectonic and dyke-induced faults.

Graben half-width and dyke depth

Graben half-width (*HW*) is commonly used to predict a dyke's depth (*D'*) beneath the surface (i.e. *D' = HW* tan *α*) [*Hjartardóttir et al.*, 2016; *Pollard et al.*, 1983; *Trippanera et al.*, 2015a]. We show *HW*, measured along horizon HF, ranges from ~366±18 m to 728±36 m (Figs 3c, d). The southern ~8 km of the graben is characterised by a mean *HW* of ~488±24 m, which abruptly increases to ~711±36 m before gradually decreasing to ~519±26 m at ~18 km (Fig. 3d). This abrupt change in *HW* is coincident with a northwards decrease in the average fault dip of EF1 and EF2 at HF (from ~56° to ~45° on HF*α*; Figs 3d). This change in HF*α* reflects variations in fault dip across the surfaces of both EF1 and EF2, with the latter broadly dipping more steeply (Fig. 3e). We use our measured *HW* and HF*α* to calculate *D'*, which ranges from ~446±46 m to ~1006±106 m; this methodology assumes fault dip remains constant with depth and is synonymous to extrapolating fault dips measured in the field[9].

Our 3D seismic data allow us to test the accuracy of predicted *D'* because we can measure dyke depth (*D*) beneath HF. We show *D* ranges from ~493±80 m to 896±134 m, and is positively, yet only weakly ($R^2 = 0.20$) correlated to *D'*, although we acknowledge there is broadly a good agreement between *D'* and *D* if error ranges are considered (Figs 3d, f). Importantly, our results indicate *D'* may occasionally exceed *D* by up to 350±145 m (Fig. 3d), implying graben properties measured at the surface may not always provide realistic constraints on dyke depth. Because *D'* is sensitive to *α* (Fig. 3g), which is typically assumed to remain constant with depth (i.e. the fault is planar) [*Hjartardóttir et al.*, 2016; *Pollard et*

al., 1983; *Trippanera et al.*, 2015a; *Wilson and Head*, 2002], the variation in dip we record

across EF1 and EF2 (Fig. 3e) may explain the observed discrepancies between *D'* and *D*. For

example, where average fault dips between horizons HE–HA (i.e. HE–HA*α*) are less than

those along the overlying HF, i.e. the difference between HF*α* and HE–HA*α* is >0, the faults

are concave-up (listric) and *D'* overestimates *D* (*D*:*D'*>1; Fig. 3h). Conversely, where faults

are convex-up and the difference between HF*α* and HE–HA*α* is <0, *D'* underestimates *D*

(*D*:*D'*<1; Fig. 3h). Offset of dyke-induced faults by cross-cutting tectonic faults can also

cause *D'* to deviate from *D* by artificially increasing (Fig. 3d) or decreasing *HW*.
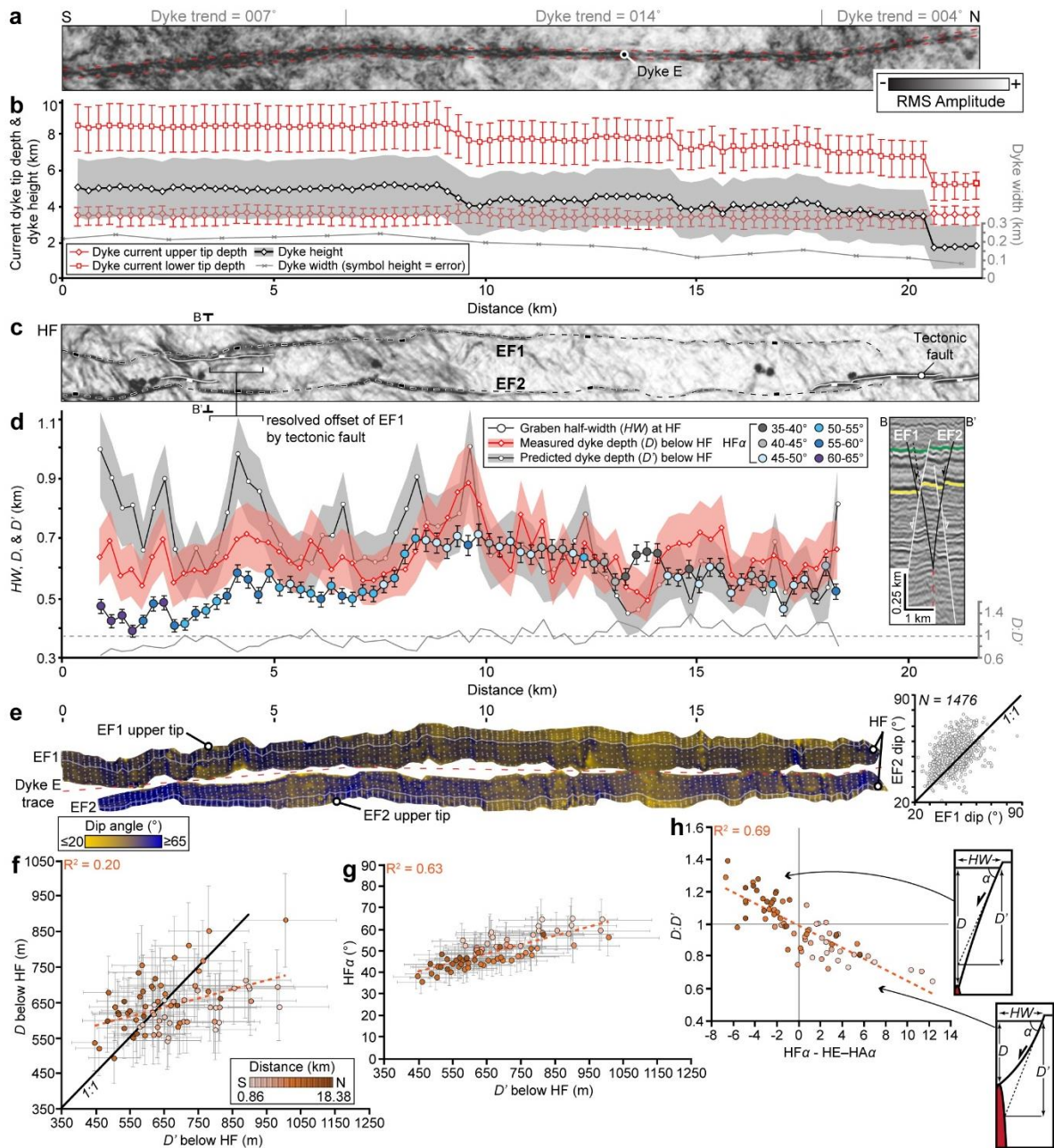
Figure 3: Plan-views and quantitative measurements of Dyke E and dyke-induced faults EF1 and EF2. **a,** RMS amplitude map of highlighting the Dyke E trace is kinked (Fig. 2a). **b,** Graph showing how dyke height, tip depths, and apparent thickness changes along-strike. All error bars, including those in **d, f,** and **g,** account for possible ±5% variability in data resulting from human error, whilst measurements reliant on depth-conversion, e.g. dyke height and tip depths, also include ±10% due to uncertainty in seismic velocities used; these latter measurements thus have ±15% error bars (see Methods for further explanation). **c,** RMS

amplitude map of HF showing variations in graben half-width (*HW*). **d,** *HW* and dip

variations at HF (HFα), as well as measured (*D*) and predicted (*D'*) dyke tip depth below HF,

plotted against distance. Error bars for *HW* are ±5% and error envelopes for *D* and *D'* are

±15%. Inset: seismic section shows tectonic faults may cut dyke-induced faults, locally

increasing *HW*. **e,** Fault dip map (see Supplementary Video 1 for a 3D view of dip maps).

Inset: Cross-plot of EF1 and EF2 dips, for coincident positions on both faults, showing EF2 is

broadly steeper dipping than EF1; error bars omitted for clarity. **f,** Plot showing *D'* may not

equal *D*; error bars are ±15%. **g,** Plot showing *D'* is sensitive to HFα; error bars are ±15%. **h,**

Plot showing that where the average dip of EF1 and EF2 below HF (HE–HAα) is less than

HFα, the fault is listric and *D'>D*. Where the lower portion of EF1 and EF2 are convex-up,

D'<D.

Dyke-induced fault displacement and kinematics

Displacement varies along-strike and down-dip of both EF1 and EF2, which have

displacement maximum of ~73±11 m and ~113±17 m, respectively (Figs 4a, d). Zones of

high displacement (e.g. S1-S4 on EF2), separated by displacement minima, are observed

across EF1 and EF2 and occur at different structural levels (Fig. 3a). For example, S4 is ~2.7

km long with a displacement maxima of ~97±15 m centred on HH, whereas the displacement

maxima in S3 occurs between HA–HD (Fig. 4a). The transition between S3 and S4 occurs

above a change in dyke trend from 007° to 014° (Fig. 4a). For the same equivalent along-

strike position, maximum displacement on both faults commonly differs, with EF2 primarily

accommodating more strain (Figs 4a, b). Cumulative heave across both EF1 and EF2 is up to

~115±17 m and broadly decreases northwards (Fig. 4c), consistent with a reduction in the

width of the low-amplitude zone marking the dyke(s) (Fig. 3b). Changes in heave between

zones of high- and low-displacement are up to ~83±22 m (i.e. S1; Fig. 3b). Displacement-

depth profiles are complex but occasionally display clear 'M-shaped' or 'C-shaped' trends (cf. Figs 1c, d, 3d)[*Muraoka and Kamata*, 1983]. Displacement maxima rarely occur at the lower tips of EF1 and EF2 and never at their upper tips (Figs 4a, d).

Dyke-induced fault displacement is intrinsically and positively linked to dyke dilation [*Rubin*, 1992; *Tryggvason*, 1984], implying variations in displacement across EF1 and EF2 (Fig. 4a) likely reflect along-strike changes in dyke thickness. Such thickness variations could be driven by localised inelastic deformation (e.g. fluidisation, thermal erosion, bridge formation) of the host rock, variations in host rock mechanical properties, and/or lateral pressure gradients generated by changes in loading conditions or magma properties (Fig. 4e) [*Delaney and Pollard*, 1981; *Gudmundsson*, 1983; *Gudmundsson et al.*, 2012; *Kavanagh and Sparks*, 2011; *Magee et al.*, 2018; *Rivalta et al.*, 2015; *Vachon and Hieronymus*, 2017]. Whilst the resolution of our data are insufficient to test these hypotheses, we consider two end-member scenarios where localized dyke thickening and fault slip occur either: (i) after dyke propagation and nucleation of EF1 and EF2 fault planes (i.e. displacement maxima and nucleation sites may not coincide); or (ii) during dyke propagation, with isolated fault segments nucleating above thicker dyke portions before linking to form the larger structures. This latter scenario is based on observations of natural, and physical and numerical modelling of tectonic normal faults [*Cartwright et al.*, 1995; *Deng et al.*, 2017], and analogue models of dyke-induced faults [*Trippanera et al.*, 2015a], which reveal zones of high displacement commonly occur where faults nucleate. Zones of high displacement on EF1 and EF2 could thus represent nucleation sites of originally isolated fault segments, with areas of lower displacement forming as these segments grew and linked [*Cartwright et al.*, 1995]. We suggest lateral propagation of a dyke could promote nucleation and rapid lengthening of an overlying fault, with areas of high displacement developing over its thickest (and highest) section (Fig. 4f) [*Trippanera et al.*, 2015a]. If the dyke stalls and pressurises, driving fault

growth as it thickens, renewed lateral propagation could be facilitated by magma breaking

and spreading out from the dyke nose [*Healy et al.*, 2018], instigating nucleation of a new,

laterally offset fault segment (Fig. 4f). Continued intrusion and dyke dilation will lead to fault

segment growth and coalescence, where sites of linkage are characterised by displacement

minima (cf. Figs 3a, 4f). Such incremental emplacement of a dyke is consistent with the 2014

Bárðarbunga dyking event, where frequent stalling of a laterally injected dyke led to

pressurization (and thickening) behind its tip, until the energy barrier inhibiting intrusion was

overcome and a new dyke segment propagated [*Sigmundsson et al.*, 2015; *Woods et al.*,
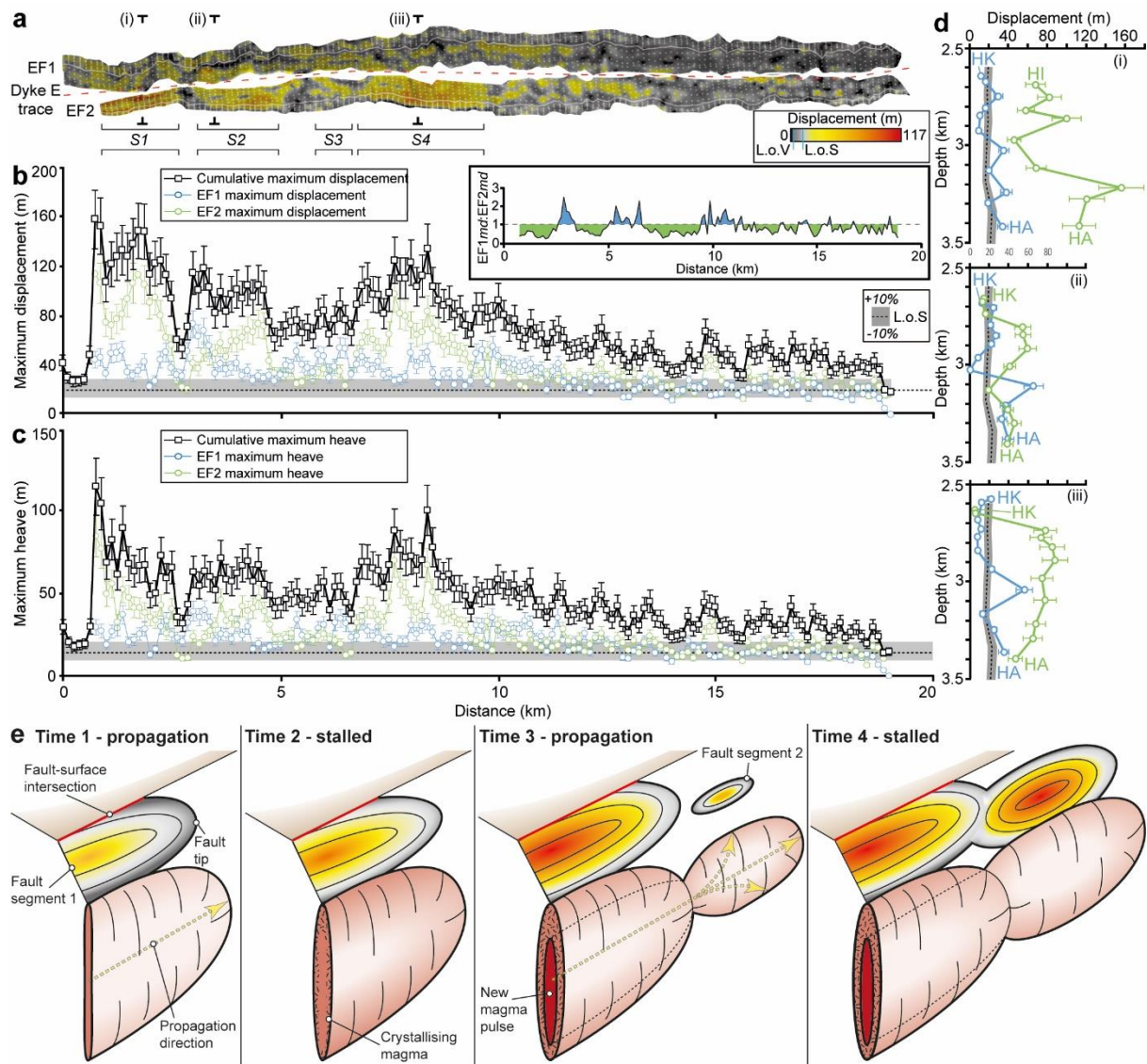
2019].

Figure 4: Displacement distribution of EF1 and EF2. **a,** Map highlighting non-uniform distribution of displacement across EF1 and EF2. Discrete zones of high displacement are recognised along fault strike, particularly on EF2 (i.e. S1–S4). Average limits of separability (L.o.S) and visibility (L.o.V) incorporated into colour-bar. See Supplementary Video 1 for a 3D view of these displacement maps. **b, c,** Plots of maximum displacement and heave along EF2 and EF2; cumulative maximum displacement and heave combining data from both faults also shown. Limit of separability (±10%) also shown. Error bars shown are ±15% and account for possible variability in measurements derived from human error (±5%) and changes in seismic velocity (±10%). See Methods for further explanation of errors. Inset in

b,: changes in ratio of EF1 maximum displacement (*md*) to EF2 maximum displacement along-strike, showing strain is differentially partitioned across the two faults. **d,** Depth-displacement profiles for EF1 and EF2; error bars are ±15%. Limit of separability (±10%) also shown. See **a,** for location. **e,** Conceptual model for how cyclical dyke propagation and stalling could promote nucleation, growth, and linkage of discrete fault segments.

Discussion

We show a natural pair of dyke-induced faults extend from the contemporaneous surface and converge on, but do not continue below, a dykes upper tip [cf. *Rowland et al.*, 2007; *Rubin and Pollard*, 1988]. Displacement varies across the dyke-induced faults, likely reflecting changes in the thickness of the underlying dyke. If zones of high-displacement along the dyke-induced faults correspond to sites where the fault nucleated [*Cartwright et al.*, 1995; *Deng et al.*, 2017; *Trippanera et al.*, 2015a], our results indicate the dyke-induced faults nucleated between the dyke and contemporaneous seabed [*Mastin and Pollard*, 1988]; this contrasts with many proposed models, which suggest dyke-induced faults nucleate either at the surface [*Al Shehri and Gudmundsson*, 2018; *Trippanera et al.*, 2015a; *Trippanera et al.*, 2015b] and/or upper dyke tip [*Al Shehri and Gudmundsson*, 2018; *Koehn et al.*, 2019; *Pollard et al.*, 1983; *Rubin*, 1992; *Rubin and Pollard*, 1988; *Tentler*, 2005; *Xu et al.*, 2016]. Regardless of where the faults nucleated, our kinematic reconstruction implies any seismicity generated by this type of dyke-induced faulting is likely to be concentrated away from the dyke upper tip, in areas where most displacement is accrued. Critically, we also demonstrate the distribution of displacement across dyke-induced faults influences their surface expression (e.g. Fig. 1), such that cumulative heave measured along the syn-intrusion surface likely does not approximate dyke thickness [*Rubin*, 1992]. Similarly, we show dyke-induced fault dip varies along-strike and down-dip, implying dyke upper tip depths estimated from

graben half-width, which commonly assume faults are planar, may be incorrect [cf.*Hjartardóttir et al.*, 2016; *Mastin and Pollard*, 1988; *Pollard et al.*, 1983; *Rubin and Pollard*, 1988; *Trippanera et al.*, 2015b]. Accurately constraining dyke parameters (e.g. thickness, depth, and volume) from the surface expression of dyke-induced faults thus requires knowledge of fault geometry and growth in 3D; unfortunately this information is commonly unavailable. Using seismic reflection data to unravel how faults grow above dykes and quantify their 3D structure can improve our understanding of dyke emplacement and its role in driving crustal extension (e.g. continental break-up) on Earth and other planetary bodies.

Methods

Seismic reflection data

The Glencoe and Chandon 3D, time-migrated seismic reflection surveys have a bin spacings of 25 m and record lengths of 8 s two-way time (TWT) and 6 s TWT, respectively. The Chandon survey is displayed with an SEG negative polarity; i.e. a trough (black) reflection corresponds to a downward increase in acoustic impedance whilst a peak (white) reflection represents a downward decrease in acoustic impedance. The Glencoe survey is displayed with an SEG positive polarity. To constrain the dykes between the two 3D seismic datasets we used 2D seismic lines from the Champagne 2D MSS and JA95 surveys. We use velocity information from local borehole data to convert the seismic data from depth in ms two-way time (TWT) to metres.

Dyke imaging

Dykes are rarely directly imaged (i.e. expressed as a discrete reflection) in seismic reflection data because their sub-vertical orientation means little energy is reflected back to and

recorded at the surface[*Thomson*, 2007]. The dykes we describe, similar to those inferred in the North Sea by *Wall et al.* [2010], are rather expressed by an absence or reduction in imaging; i.e. less energy is reflected from the stratigraphic horizons where they are intersected by dykes, meaning their lateral continuity is disrupted [*Eide et al.*, 2018]. Changes to the mechanical properties of wall rock adjacent to dykes by contact metamorphism of the wall rock may also influence energy reflection, potentially increasing the width of the low-amplitude zones centred on the dykes [*Wall et al.*, 2010]. The geophysical expression of the dykes is, thus, technically a vertical seismic artefact, the width of which does not necessarily correspond to dyke thickness [*Wall et al.*, 2010]. However, we suggest that relative changes in the along-strike width of the low-amplitude zones of disruption mimic relative variations in dyke thickness. The observed northwards thinning of the low-amplitude zones marking the dyke and a northwards decrease in heave, another proxy for dyke thickness[*Rubin and Pollard*, 1988], supports our inference that the geophysical expression of the dykes can be related to their geometry.

Borehole data

Seven boreholes were used to tie mapped horizons between the datasets and determine their age: Mercury-1, Yellowglen-1, Chandon-1, Chandon-2, Chandon-3, Toporoa-1, and Cloverhill-1. To depth-convert the Chandon 3D survey around the studied dyke-induced faults and the upper dyke tips, we used checkshot and horizon depth data from Mercury-1, Yellowglen-1, Chandon-1, Chandon-2, and Chandon-3 (Supplementary Table 1). Specifically, we calculated interval velocities between the seabed, Top Muderong Formation, Top Mungaroo Formation, and down to 4 s TWT; we assumed a velocity of 1.5 km s^{-1} for the water column (Supplementary Table 1). Conversion of dyke base depth measurements from s TWT to metres, which occurs below the limits of our depth-conversion, was conducted by

extrapolating a second order polynomial trend-line, through the cumulative checkshot data of the five wells (Supplementary Table 1), defined by the equation:

$$y = 919.51x^2 + 23.88x + 626.46.$$

Seismic Resolution

Between the top of the dyke-induced faults (~2.9 s TWT or ~2.6 km) and the approximate middle of the dykes (~4.5 s TWT; ~5.3 km), we used velocity data defined from the boreholes and measurements of average dominant frequency across three inlines to calculate the vertical and horizontal resolution of the data; the base of the dyke-induced faults occurs at ~3.5 s TWT or ~3.5 km. We specifically define the vertical resolution as the limits of separability ($\lambda/4$, where λ is the seismic wavelength) and visibility ($\lambda/30$); i.e. the minimum thickness of a layer where reflections from its top and base can be distinguished defines the limit of separability [*Brown*, 2011]. The limit of visibility defines the thickness at which a layer can be distinguished from background noise in the seismic reflection data[*Brown*, 2011]. A layer with a thickness between the limits of separability and visibility is characterised by a tuned reflection package, created when reflections from its top and base interfere on their way to the surface and cannot be deconvolved[*Brown*, 2011].

We measured the dominant frequency and interval velocity for every 0.1 s TWT increments, from 2.8–4.5 s TWT, to quantify changes in resolution with depth (Supplementary Table 2). To account for potential variability in interval velocities, which may arise due to lateral changes in lithology away from the boreholes, we consider interval velocities have ±10% errors (Supplementary Table 2). We show the data resolution broadly decreases with depth (Supplementary Table 2). For the strata hosting the dyke-induced faults, the minimum and maximum limits of separability are ~14 m and 29 m, respectively; the

average limits of separability and visibility are ~20 m and ~3 m, respectively (Supplementary Table 2).

Quantitative analysis

We selected faults EF1 and EF2 for displacement distribution analysis because they are continuous along-strike and their northernmost lateral tips are captured in the seismic reflection data. Compared to other dyke-induced faults, which are segmented, show subtle curvature along-strike, and/or interact with highly oblique tectonic normal faults, EF1 and EF2 appear to represent the simplest faults (Fig. 1).

Eleven sedimentary horizons (i.e. horizons HA–HK; Fig. 1c) from different structural levels were mapped locally around EF1 and EF2 and their hanging wall and footwall cut-offs were mapped as points every 125 m along-strike. In some sections, mapped horizons appear folded adjacent to the faults, which may reflect evidence of ductile strain during deformation; we accounted for this by projecting the regional trend of the strata to define cut-offs [*Mansfield and Cartwright*, 1996]. For each cut-off pair, we manually measured fault throw and extracted fault dip information; this data was used to calculate fault heave and displacement (Supplementary Table 3). Fault dip data were specifically extracted by creating dip angle maps from depth-converted fault surfaces constructed using all footwall cut-offs mapped along HA–HK (~1500 per fault). The convergent interpolation gridding algorithm in Schlumbergers's Petrel seismic interpretation software was used to grid these data into a surface; this algorithm applies a linear projection to extrapolate between points and a 'trend' method to preserve data trends.

Because the maximum fault heave is a proxy for dyke thickness[*Rubin and Pollard*, 1988], plots of heave variation along-strike (i.e. Fig. 3d) use the maximum heave on any given vertical transect along-strike; i.e. neighbouring heave data-points may not have been

measured on the same horizon. Graben width was measured every 125 m along-strike on Horizon HF; although this horizon does not mark the top of the fault, it is the uppermost prominent reflection that F1 and F2 displace along their entire lengths. Dyke tip depths, used to calculate dyke height, and width of the dykes geophysical expression were measured every 250 m along-strike.

Sources of error

There are several sources of error affecting confidence in quantitative measurements obtained from seismic reflection data [*Brown*, 2011]. The primary error source relates to seismic velocities used to convert the seismic data and measurements from depth in seconds two-way time (TWT) to depth in metres. This uncertainty arises because seismic velocities are obtained from borehole data, which effectively only provide a 1D snapshots of the subsurface geology and may thus not capture lateral variations in rock properties and seismic velocity. The numerous wells in our study area all display similar time-depth relationships, which indicates seismic velocities remain relatively constant laterally (Supplementary Figure 2). We thus take a conservative view that calculated seismic velocities vary by up to ±10%. Measurements of limits of separability and visibility, fault cut-offs, fault dips, dyke upper tip, and dyke lower tip depths rely on depth-converting time data and are therefore considered to have errors of ±10%. We also acknowledge that manual mapping and measurement can introduce human errors; we cannot quantify these errors but conservatively assume they could be up to ±5%. Data for graben half-width (*HW*) and dyke width are thus presented with ±5% errors as they do not rely on depth-converting any measurements, whilst the dykes lower and upper tip depths (including *D* and *D'*), fault dips, displacement, and heave assume errors are ±15%. We do not calculate errors for ratios. Fault displacement and dip maps may

also contain interpolation errors derived from our choice gridding algorithms, but we consider these negligible given the high density of measurement locations across both faults.

Data Availability

The seismic reflection and borehole data used (see text for details) are publically available through Geoscience Australia at http://www.ga.gov.au/nopims. Videos of the 3D seismic volume used to generate the dyke-induced fault displacement maps can be found at https://figshare.com/ (DOI: 10.6084/m9.figshare.7623779). All other relevant data, including borehole checkshot data, seismic resolution data, and fault parameter (e.g., displacement and dip) data are provided as Supplementary Tables.

Author contributions

CM designed the project, analysed data, led interpretation, and wrote the manuscript. CALJ acquired the data, aided interpretation, and edited the manuscript.

Competing interests

The authors declare no competing interests.

References

Al Shehri, A., and A. Gudmundsson (2018), Modelling of surface stresses and fracturing during dyke emplacement: Application to the 2009 episode at Harrat Lunayyir, Saudi Arabia, *Journal of Volcanology and Geothermal Research*, *356*, 278-303.

Bosworth, W., D. F. Stockli, and D. E. Helgeson (2015), Integrated outcrop, 3D seismic, and geochronologic interpretation of Red Sea dike-related deformation in the Western Desert, Egypt– The role of the 23Ma Cairo "mini-plume", *Journal of African Earth Sciences*, *109*, 107-119.

Brown, A. R. (2011), *Interpretation of three-dimensional seismic data*, 6th ed., 534 pp., AAPG and SEG, Oklahoma, USA.

Carbotte, S. M., R. S. Detrick, A. Harding, J. P. Canales, J. Babcock, G. Kent, E. Van Ark, M. Nedimovic, and J. Diebold (2006), Rift topography linked to magmatism at the intermediate spreading Juan de Fuca Ridge, *Geology*, *34*(3), 209-212.

Cartwright, J. A., B. D. Trudgill, and C. S. Mansfield (1995), Fault growth by segment linkage: an explanation for scatter in maximum displacement and trace length data from the Canyonlands Grabens of SE Utah, *Journal of Structural Geology*, *17*(9), 1319-1326.

Delaney, P. T., and D. D. Pollard (1981), Deformation of host rocks and flow of magma during growth of minette dikes and breccia-bearing intrusions near Ship Rock, New Mexico*Rep. 2330-7102*, USGPO.

Deng, C., R. L. Gawthorpe, E. Finch, and H. Fossen (2017), Influence of a pre-existing basement weakness on normal fault growth during oblique extension: Insights from discrete element modeling, *Journal of Structural Geology*, *105*, 44-61.

Driscoll, N. W., and G. D. Karner (1998), Lower crustal extension across the Northern Carnarvon basin, Australia: Evidence for an eastward dipping detachment, *Journal of Geophysical Research: Solid Earth (1978–2012)*, *103*(B3), 4975-4991.

Dumont, S., A. Socquet, R. Grandin, C. Doubre, and Y. Klinger (2016), Surface displacements on faults triggered by slow magma transfers between dyke injections in the 2005–2010 rifting episode at Dabbahu–Manda–Hararo rift (Afar, Ethiopia), *Geophysical Journal International*, *204*(1), 399-417.

Dumont, S., Y. Klinger, A. Socquet, C. Doubre, and E. Jacques (2017), Magma influence on propagation of normal faults: Evidence from cumulative slip profiles along Dabbahu-Manda-Hararo rift segment (Afar, Ethiopia), *Journal of Structural Geology*, *95*, 48-59.

Eide, C. H., N. Schofield, I. Lecomte, S. J. Buckley, and J. A. Howell (2018), Seismic Interpretation of Sill-complexes in Sedimentary Basins: The 'sub-sill Imaging Problem', *Journal of the Geological Society*, *175*, 193-209.

Exon, N., U. Von Rad, and U. Von Stackelberg (1982), The geological development of the passive margins of the Exmouth Plateau off northwest Australia, *Marine Geology*, *47*(1-2), 131-152.

Gudmundsson, A. (1983), Form and dimensions of dykes in eastern Iceland, *Tectonophysics*, *95*(3-4), 295-307.

Gudmundsson, A., S. Kusumoto, T. H. Simmenes, S. L. Philipp, B. Larsen, and I. F. Lotveit (2012), Effects of overpressure variations on fracture apertures and fluid transport, *Tectonophysics*, *581*, 220-230.

Hardy, S. (2016), Does shallow dike intrusion and widening remain a possible mechanism for graben formation on Mars?, *Geology*, *44*(2), 107-110.

Healy, D., R. Rizzo, M. Duffy, N. J. Farrell, M. J. Hole, and D. Muirhead (2018), Field evidence for the lateral emplacement of igneous dykes: Implications for 3D mechanical models and the plumbing beneath fissure eruptions, *Volcanica*, *1*(2), 20.

Hjartardóttir, Á. R., P. Einarsson, M. T. Gudmundsson, and T. Högnadóttir (2016), Fracture movements and graben subsidence during the 2014 Bárðarbunga dike intrusion in Iceland, *Journal of Volcanology and Geothermal Research*, *310*, 242-252.

Kavanagh, J., and R. S. J. Sparks (2011), Insights of dyke emplacement mechanics from detailed 3D dyke thickness datasets, *Journal of the Geological Society*, *168*(4), 965-978.

Koehn, D., A. Steiner, and K. Aanyu (2019), Modelling of extension and dyking-induced collapse faults and fissures in rifts, *Journal of Structural Geology*, *118*, 21-31.

Maccaferri, F., E. Rivalta, L. Passarelli, and Y. Aoki (2016), On the mechanisms governing dike arrest: Insight from the 2000 Miyakejima dike injection, *Earth and Planetary Science Letters*, *434*, 64-74.

Magee, C., R. E. Ernst, J. Muirhead, T. Phillips, and C. A.-L. Jackson (2019), Magma Transport Pathways in Large Igneous Provinces: Lessons from Combining Field Observations and Seismic Reflection Data, in *Dyke Swarms of the World: A Modern Perspective*, edited by R. Srivastava, R. Ernst and P. Peng, pp. 45-85, Springer.

Magee, C., J. Muirhead, N. Schofield, R. J. Walker, O. Galland, S. Holford, J. Spacapan, C. A. Jackson, and W. McCarthy (2018), Structural signatures of igneous sheet intrusion propagation, *Journal of Structural Geology*.

Mansfield, C. S., and J. A. Cartwright (1996), High resolution fault displacement mapping from three-dimensional seismic data: evidence for dip linkage during fault growth, *Journal of Structural Geology*, *18*, 14.

Mastin, L. G., and D. D. Pollard (1988), Surface deformation and shallow dike intrusion processes at Inyo Craters, Long Valley, California, *Journal of Geophysical Research: Solid Earth*, *93*(B11), 13221-13235.

Muraoka, H., and H. Kamata (1983), Displacement distribution along minor fault traces, *Journal of Structural Geology*, *5*(5), 483-495.

Pallister, J. S., W. A. McCausland, S. Jónsson, Z. Lu, H. M. Zahran, S. El Hadidy, A. Aburukbah, I. C. Stewart, P. R. Lundgren, and R. A. White (2010), Broad accommodation of rift-related extension recorded by dyke intrusion in Saudi Arabia, *Nature Geoscience*, *3*(10), 705.

Passarelli, L., E. Rivalta, S. Cesca, and Y. Aoki (2015), Stress changes, focal mechanisms, and earthquake scaling laws for the 2000 dike at Miyakejima (Japan), *Journal of Geophysical Research: Solid Earth*, *120*(6), 4130-4145.

Phillips, T. B., C. Magee, C. A.-L. Jackson, and R. E. Bell (2018), Determining the three-dimensional geometry of a dike swarm and its impact on later rift geometry using seismic reflection data, *Geology*, *46*(2), 119-122.

Pollard, D. D., P. T. Delaney, W. A. Duffield, E. T. Endo, and A. T. Okamura (1983), Surface deformation in volcanic rift zones, *Tectonophysics*, *94*(1-4), 541-584.

Reeve, M. T., C. A. L. Jackson, R. E. Bell, C. Magee, and I. D. Bastow (2016), The stratigraphic record of prebreakup geodynamics: Evidence from the Barrow Delta, offshore Northwest Australia, *Tectonics*, *35*(8), 1935-1968.

Rivalta, E., B. Taisne, A. Bunger, and R. Katz (2015), A review of mechanical models of dike propagation: Schools of thought, results and future directions, *Tectonophysics*, *638*, 1-42.

Rowland, J., E. Baker, C. Ebinger, D. Keir, T. Kidane, J. Biggs, N. Hayward, and T. Wright (2007), Fault growth at a nascent slow-spreading ridge: 2005 Dabbahu rifting episode, Afar, *Geophysical Journal International*, *171*(3), 1226-1246.

Rubin, A. M. (1992), Dike-induced faulting and graben subsidence in volcanic rift zones, *Journal of Geophysical Research: Solid Earth*, *97*(B2), 1839-1858.

Rubin, A. M., and D. D. Pollard (1988), Dike-induced faulting in rift zones of Iceland and Afar, *Geology*, *16*(5), 413-417.

Ruch, J., T. Wang, W. Xu, M. Hensch, and S. Jónsson (2016), Oblique rift opening revealed by reoccurring magma injection in central Iceland, *Nature communications*, *7*, 12352.

Schultz, R. A., C. H. Okubo, C. L. Goudy, and S. J. Wilkins (2004), Igneous dikes on Mars revealed by Mars orbiter laser altimeter topography, *Geology*, *32*(10), 889-892.

Sigmundsson, F., A. Hooper, S. Hreinsdóttir, K. S. Vogfjörd, B. G. Ófeigsson, E. R. Heimisson, S. Dumont, M. Parks, K. Spaans, and G. B. Gudmundsson (2015), Segmented lateral dyke growth in a rifting event at Bárðarbunga volcanic system, Iceland, *Nature*, *517*(7533), 191.

Symonds, P. A., S. Planke, O. Frey, and J. Skogseid (1998), Volcanic evolution of the Western Australian Continental Margin and its implications for basin development, *The Sedimentary Basins of Western Australia 2: Proc. of Petroleum Society Australia Symposium, Perth, WA*.

Tentler, T. (2005), Propagation of brittle failure triggered by magma in Iceland, *Tectonophysics*, *406*(1), 17-38.

Thomson, K. (2007), Determining magma flow in sills, dykes and laccoliths and their implications for sill emplacement mechanisms, *Bull Volcanol*, *70*(2), 183-201.

Trippanera, D., J. Ruch, V. Acocella, and E. Rivalta (2015a), Experiments of dike-induced deformation: Insights on the long-term evolution of divergent plate boundaries, *Journal of Geophysical Research: Solid Earth*, *120*(10), 6913-6942.

Trippanera, D., V. Acocella, J. Ruch, and B. Abebe (2015b), Fault and graben growth along active magmatic divergent plate boundaries in Iceland and Ethiopia, *Tectonics*, *34*(11), 2318-2348.

Tryggvason, E. (1984), Widening of the Krafla fissure swarm during the 1975–1981 volcano-tectonic episode, *Bull Volcanol*, *47*(1), 47-69.

Vachon, R., and C. F. Hieronymus (2017), Effect of host-rock rheology on dyke shape, thickness and magma overpressure, *Geophysical Journal International*, *208*(3), 1414-1429.

Wall, M., J. Cartwright, R. Davies, and A. McGrandle (2010), 3D seismic imaging of a Tertiary Dyke Swarm in the Southern North Sea, UK, *Basin Research*, *22*(2), 181-194.

Wilson, L., and J. W. Head (2002), Tharsis-radial graben systems as the surface manifestation of plume-related dike intrusion complexes: Models and implications, *Journal of Geophysical Research: Planets*, *107*(E8).

Woods, J., T. Winder, R. S. White, and B. Brandsdóttir (2019), Evolution of a lateral dike intrusion revealed by relatively-relocated dike-induced earthquakes: The 2014–15 Bárðarbunga–Holuhraun rifting event, Iceland, *Earth and Planetary Science Letters*, *506*, 53-63.

Wright, T. J., F. Sigmundsson, C. Pagli, M. Belachew, I. J. Hamling, B. Brandsdóttir, D. Keir, R. Pedersen, A. Ayele, and C. Ebinger (2012), Geophysical constraints on the dynamics of spreading centres from rifting episodes on land, *Nature Geoscience*, *5*(4), 242-250.

Xu, W., S. Jónsson, F. Corbi, and E. Rivalta (2016), Graben formation and dike arrest during the 2009 Harrat Lunayyir dike intrusion in Saudi Arabia: Insights from InSAR, stress calculations and analog experiments, *Journal of Geophysical Research: Solid Earth*, *121*(4), 2837-2851.